



## High-throughput and label-free screening of red blood cell stiffness: A study of sickle cell disease

Saurabh Kaushik<sup>a</sup>, Arkabrata Mishra<sup>a</sup>, Roshan Ross<sup>b</sup>, Sweta Srivastava<sup>b</sup>, Cecil R. Ross<sup>b</sup>, Gautam V. Soni<sup>a,\*</sup> 

<sup>a</sup> Raman Research Institute, Bangalore, 560080, India

<sup>b</sup> St. Johns Medical College Hospital, Bangalore, 560034, India

### ARTICLE INFO

#### Keywords:

Resistive pulse sensing  
Electro fluidics  
Sickle cell disease  
Cellular elasticity  
Red blood cells  
Atomic force microscopy

### ABSTRACT

Understanding the morphological and mechanical changes in cells are important for diagnostic and treatment methods in various diseases. In sickle cell disease (SCD), the mutated hemoglobin (HbS) aggregates inside the red blood cells (RBCs), making them rigid and, in extreme cases, sickle-shaped, resulting in anemia, episodes of pain, and multiple organ damage. Existing techniques are too costly and insensitive since the effect of the HbS gene (heterozygous and homozygous) is variable both in prevalence and clinical manifestations. In this work, we present a label-free, cost-effective, high-throughput electro-fluidic technique to study changes in the mechanical and morphological characteristics of RBCs. We validate our device by quantitatively comparing the mechanical properties of RBCs as a function of stiffness-altering drug (Latrunculin-A) with measurements using AFM. We demonstrate the on-site application of our system by screening SCD patients based on their RBC stiffness changes. The signatures of patient-specific heterogeneity in the RBC mechanical properties may help in monitoring clinical variability and identification of high-risk patients along with targeted therapies. The versatility of our measurements opens the whole cell stiffness as a preliminary screening biomarker in other haematological conditions, tumor cell identification, in veterinary sciences as well as in evaluating hydrogel technologies.

### 1. Introduction

About 300,000 babies are born every year with sickle cell disease (SCD) or anemia, globally. SCD cases are found all across the world with most cases reported in Nigeria, the Democratic Republic of the Congo, and India (Kato et al., 2018; Obeagu et al., 2015; Stanley Davidson, 2014). Among other countries, SCD has majorly affected India's southern-central rural regions, due to which the Indian Government has announced the 'National Sickle Cell Anaemia Elimination Mission' (MoHFW, 2023) for its eradication. Sickle cell disease is a group of genetic disorders caused by at least a 1-point mutation of the Hemoglobin  $\beta$ -globin (HBB) gene (Kato et al., 2018; Obeagu et al., 2015; Liu et al., 2017, 2018, 2019; Tewari and Rees, 2013; Desai and Dhanani, 2012; Arishi et al., 2021; Serjeant, 2013). The mutated hemoglobin proteins can form a long polymeric chain, then causing aggregates inside the red blood cells, making them rigid and sickle-shaped (Kato et al., 2018; Obeagu et al., 2015; Liu et al., 2018, 2019; Desai and Dhanani, 2012; Arishi et al., 2021; Ilyas et al., 2020). The deformability,

self-aggregation, and adherence of RBCs to the endothelial cells of the blood vessel walls have been a prominent factor for blood vessel occlusion (vaso-occlusions) during microcirculation. In SCD patients, the stiffened RBCs, cause severe vaso-occlusion of the blood flow and the RBCs break apart quickly. The mean life span of RBCs reduces to 17 days from their natural life span of 120 days (Obeagu et al., 2015), which causes the state of anemia. The interruption of blood flow and the anemia cause episodes of chronic pain and multiple organ damage respectively (Kato et al., 2018; Obeagu et al., 2015; Liu et al., 2018, 2019; Tewari and Rees, 2013; Ilyas et al., 2020; Rees et al., 2022; Shah et al., 2020; Marcus et al., 1997). There are multiple types of SCD, the specific type depends on which HBB gene mutation was inherited from the parents. A few common SCDs are HbAS, HbSC, HbS  $\beta$ -thalassemia, HbSD, HbSE, and HbSO. Here, 'A' represents the normal hemoglobin gene, whereas, 'S', 'C', 'D', 'E', and 'O' represent the abnormal hemoglobin genes (Kato et al., 2018; Obeagu et al., 2015; Stanley Davidson, 2014; Arishi et al., 2021; Serjeant, 2013). It is also important to note that, the sickling phenomenon in most of the SCD types mentioned

\* Corresponding author.

E-mail address: [gvsoni@rri.res.in](mailto:gvsoni@rri.res.in) (G.V. Soni).

above is enhanced in the oxygen-deprivation state (Kato et al., 2018; Obeagu et al., 2015; Liu et al., 2017, 2018, 2019; Desai and Dhanani, 2012; Arishi et al., 2021; Ilyas et al., 2020; Rees et al., 2022; Shah et al., 2020).

Although, there are numerous treatment drugs and medical procedures available for sickle cell patients (Alli and Loonat, 2010; Ou and Rognerud, 2001; Albertolle, 2017; Abdel-et al., 2023; Brandow and Liem, 2022; Ndefo et al., 2008), one of the crucial challenges in dealing with this genetic disease is the screening of a large population for SCD markers. Peripheral blood smear, solubility sickling test, isoelectric focusing, Lateral Flow Immunoassay, and high-performance liquid chromatography (HPLC) are the currently available commercial techniques for sickle cell disease diagnosis (Arishi et al., 2021; Alli and Loonat, 2010; Albertolle, 2017). Among all, HPLC is a test that detects various variants of hemoglobin, and considered the most accurate diagnostic tool for sickle cell patients, and is preferred by hematologists (Ou and Rognerud, 2001; Fisher et al., 1997). This method, however, is incompatible and quite expensive to be used for population-wide screening of SCD. These sickle cell anemia patients and carriers have coexisting iron and other deficiencies, which are not picked up by HPLC. Hence the mechanical and morphological indices of red blood cells may be able to identify the high-risk SCD patients who might have other asymptomatic underlying conditions (Bhatia and Rao, 1986). Considering the limitations, a better label-free diagnostic platform is needed for the preliminary screening of patients showing hematological anomalies that can indicate sickle cell conditions.

There have been recent reports of the characterization of cell's mechanical and rheological properties using different detection methodologies (Nyberg et al., 2016, 2017; Adamo et al., 2012; Tsai et al., 2014; Ito and Kaneko, 2020; Urbanska et al., 2020; Gossett et al., 2012; Otto et al., 2015; Byun et al., 2013; Raj and Sen, 2018). Most microfluidic-based detection systems have reported on in-direct parameters, such as longitudinal and/or lateral strains (Urbanska et al., 2020; Gossett et al., 2012; Otto et al., 2015), dimensionless deformability parameters (Tsai et al., 2014), and/or transit times (Ito and Kaneko, 2020; Byun et al., 2013; Raj and Sen, 2018) to correlate measured parameters to the mechanical property of the cells. Various research techniques are capable of measuring physical parameters of the cell, either with great sensitivity (optical tweezers and AFM) or throughput (micropipette aspiration, hydrodynamic stretching). These techniques are, however, prohibitive in cost, need specialized training and are incompatible for in-field use (Sinha et al., 2025). Our electrofluidics based measurements provides advantages towards sensitivity, low cost as well as point-of-care form factor. Recent research works have addressed the use of resistive pulse sensing in detecting the cellular stiffness (Adamo et al., 2012; Kim et al., 2018), and reviewed the application of microfluidic systems to study the sickle cell RBCs (Ji et al., 2024; Aich et al., 2021). Our electro-fluidic system, presented here, reports direct calibration of cell stiffness (in kPa) while maintaining high resolution and throughput. We present this calibrated estimate of cellular stiffness using our label-free, cost-effective, high-throughput quantitative electro-fluidic platform. To establish the detection principle of our platform, we use Latrunculin-A (Lat-A) (actin inhibitor drug) treated RBCs to artificially and controllably soften the RBC samples taken from otherwise healthy donors. We then quantitatively relate our electro-fluidic measurement parameters to the cell stiffness by simultaneous comparison with single-cell AFM force spectroscopy measurements. Our experiments were also calibrated for parameters like cellular volume, sample incubation time & temperature, fluid flow rates, and device geometry, enabling an analytical understanding of our measurements. Finally, we demonstrate on-site applications of our platform by screening the RBCs of SCD patients at the local hospital. We show distinct signals, based on their RBC stiffness, that allow us to categorically separate the RBCs of SCD patients from the control group. Here we also show a weak correlation between RBC stiffness and the pathology lab-measured HbS content in the RBCs of SCD patients. We present our

technique as a platform for preliminary screening for SCD detection before a confirmatory HPLC test. The "whole cell stiffness" (WCS) has been an overlooked parameter in the diagnostics industry, primarily due to a lack of resolution and high throughput. We propose that our technique can be a promising platform for preliminary screening for various hematological conditions, tumor cell identification, veterinary sciences, and hydrogel technologies.

## 2. Materials and methods

### 2.1. Micropore device fabrication

Borosilicate capillaries (OD = 1 mm, ID = 0.5 mm, length = 75 mm) (Sutter Instrument) are used to fabricate micropores. Two types of devices were fabricated in this work: first type of devices with large micropores (pore dia ( $D_p$ ) > cell size) for free-flight experiments and the second type with small micropores (pore dia < cells size) for constricted-flight experiments. The glass capillaries were cleaned by ultrasonication in ethanol, acetone, and then ethanol for 2 min each. We then used a micropipette puller (Model P – 2000, Sutter Instrument) with the following parameters to pull the cleaned capillaries: Heat: 350, Filament: 0, Velocity: 25, Delay: 150, Pull: 200. For a free-flight micropore a conventional 'V-shaped' filament is mounted on a flame polisher instrument (MF – 900, Micro Forge, Narshige), to heat-shrink the pulled capillaries further to a desired dimension ( $D_p$  > cell size). For devices with a long-constricted micropore, we mounted an 'omega-shaped' ( $\Omega$ ) filament on the flame polisher instrument to shrink the pulled capillaries to our desired micropore dimensions ( $D_p$  < cell size). Then the omega-shaped ( $\Omega$ ) filament is replaced with the conventional 'V-shaped' filament to cut the glass capillary's extra front region and, flame polish the cut region. See Fig. S1 for the images of the two types of filaments and the steps involved in fabricating these micropores. The images of all the free-flight and constricted-flight micropores used in this work are shown in Figs. S2–S4. After flame polishing, it was also ensured that the micropores remained circularly symmetric before mounting them in a glass-bottom Teflon fluid chamber (~250  $\mu$ L) using curable silicone glue. The pore diameter ( $D_p$ ) was estimated from the smallest opening in the side-view optical image of the pore cross-section. The micropore was then connected to a syringe pump (Picoplus Elite, Harvard Apparatus), using a PTFE tubing to generate stable fluid flow.

### 2.2. Sample preparation

The blood samples for the study were acquired from human volunteers and SCD patients with approval from institutional ethics committee. For experiments, about 10  $\mu$ L of the whole blood (from a finger prick) was diluted by adding 500  $\mu$ L of RPMI-1640 (RPMI buffer, Sigma #SLBT0197) (pH = 7.4). The solution was then centrifuged three times at 600 rcf for 3 min at 4°C, and the RBCs were isolated from blood plasma and other cells, followed by resuspension of the RBC pellets in 1500  $\mu$ L of RPMI (Sample stock concentration). After the isolation step for every experiment, RBCs were checked for health and debris under an optical microscope.

To measure drug-dependent changes in cell stiffness, aliquots of the actin depolymerizing drug Latrunculin A (Lat-A) (Cat# L5163, Sigma) were made in DMSO buffer to 1 mM stock concentration. An appropriate concentration of this aliquot was then used to treat the RBCs for different experiments in our study (see text). We incubated the cells in Lat-A for at least 5 min at room temperature before performing the experiments.

For AFM-based force spectroscopy experiments on RBC cells, we first made a 100  $\mu$ L circular fluid cell using silicone glue on a glass slide (see Fig. S5). This glass slide was cleaned by ultra-sonication in 20 % Extran (Part# 34022090-5L Merck), ultrapure water twice (Milli-Q, Millipore), acetone, and ethanol for 5 min each. The glass slide was finally rinsed with ultrapure water to make sure there is no leftover ethanol from the last cleaning step. We then used Nitrogen to dry the fluid cell completely

and immediately added 50  $\mu\text{L}$  drop of 0.001 % PLL for 30 min incubation on the glass surface. We then removed the PLL using vacuum line and immediately added 50  $\mu\text{L}$  of RBC sample stock and incubated it for 30 min. The fluid cell was then gently washed with 3–5 mL of fresh RPMI buffer to make sure that all the floating cells were removed. After all these steps, the fluid cell is checked for RBC adherence under an optical microscope and then force spectroscopy measurements are performed using the AFM. The stiffness of the red blood cells can vary with temperature and storage time (Xu et al., 2018, 2019). Although the stiffness is constant up to 150 min when stored at room temperature (see Fig. S6), to ensure reproducibility, we performed all our electrofluidic experiments within 15–30 min of the blood draw.

### 2.3. Electro-fluidic measurements

The fluid cell design and experiment procedure is described elsewhere in detail (Kaushik et al., 2020, 2022). Briefly, microcapillary with the micropore at its tip was filled with RPMI buffer and glued on the fluid chamber. A PTFE tubing was connected at the back of the capillary to a syringe pump. RPMI buffer was filled in the glass bottom fluid chamber, micro-capillary, and microfluidic PTFE tubing avoiding air bubbles everywhere. The RPMI buffer works as the electrolyte for ionic current measurements through our device. A pair of Ag/AgCl electrodes, on either side of the micropore, were used to acquire the current signals, one dipped in the Teflon fluid chamber and the other inserted in the tubing. A syringe pump (in withdraw mode) was used to pull samples into the micropore device maintaining a constant fluid flow (500 nL/min). Image of a typical electrofluidic device used in this study, with the schematic of electrical connections and syringe pump is shown in Fig. S5. The device was kept inside an aluminum Faraday cage to reduce electrical noise. Low noise amplifier AM Systems (Model 2400), with 40 kHz bandwidth, and Dagan Chem-Clamp with 10 kHz bandwidth are used in this study, to apply a voltage across the devices and record the open pore current and translocation events. A noise eliminator (Hum-Bug, Quess Scientific) was also used to eliminate the input source line frequencies in the signal. Data acquisition cards from National Instruments were used to acquire and store the signals using a custom-written LabVIEW code. All the experiments performed in the lab and the hospital, used NI PCIe-6363 and NI myDAQ data acquisition cards respectively, with data sampling done at 100 kHz. The recorded data was then low pass filtered at 10 kHz and analyzed using an offline custom-written LabVIEW code. A representative quantification of an

event showing the drop in conductance ( $\Delta G$ ) and the dwell time ( $\Delta t$ ) of a recorded electrical event is shown in Fig. 1c. The  $\Delta G$  values in free-flight micropores are used to quantify any physiological changes in RBCs (Kaushik et al., 2020) as shown in the schematic Fig. 1d. In contrast, the  $\Delta t$  values from the constricted micropores indicate a change in the cellular stiffness as represented in Fig. 1e. A more detailed quantitative estimation of the cellular stiffness is later in the text. The constricted-flight and free-flight experiments were performed on patient RBC samples simultaneously to avoid any aging effects. The equivalence of the two separate amplifiers used in this study was independently confirmed (see Fig. S7). All datasets shown in this study are measured in triplicate (on same pore and same sample) and their mean and error of mean values of  $\Delta G$  and  $\Delta t$  histograms is plotted. The throughput of our technique is discussed in Figs. S7e–S7h.

### 2.4. Changes in RBC stiffness using Lat-A

For experiments with controlled changes in RBC cell stiffness, the cells were incubated in RPMI buffer with appropriate concentration (see text) of the Latrunculin-A (Lat-A) drug. All stiffness comparison experiments were performed on the same device. The sample fluid chamber was washed thoroughly with 3–5 mL of filtered RPMI in between experiments with different drug concentrations ensuring no RBCs were left from the previous experiment.

### 2.5. AFM-based cell stiffness measurements

We used an MFP-3D Infinity Bio (Asylum Research AFM, Oxford Instruments) AFM mounted on an IX73 inverted Olympus microscope for cell stiffness measurements of RBCs. Contact mode silicon nitride cantilevers attached with a spherical polystyrene bead of 4.5  $\mu\text{m}$  diameter (PT.PS.SN.4.5, Novascan) were used for taking F-X curves in this study. RBCs were adhered on the glass substrate fluid cells as briefed previously and the AFM tip was optically positioned on the RBC for every measurement. The RPMI buffer in the fluid cell was then gently washed with 1 mL (20 steps of 50  $\mu\text{L}$  each) RPMI with the appropriate Lat-A concentration needed for the study. This step was repeated for all the different Lat-A concentrations. It is important to note that another camera with a 60X objective was used to visually ensure the same cell was probed for all the Lat-A concentrations (see Fig. S8). A schematic of a spherical bead attached to a cantilever probing a soft sample is shown in Fig. S9 along with the cantilever's piezo position ( $z$ ), deflection of the

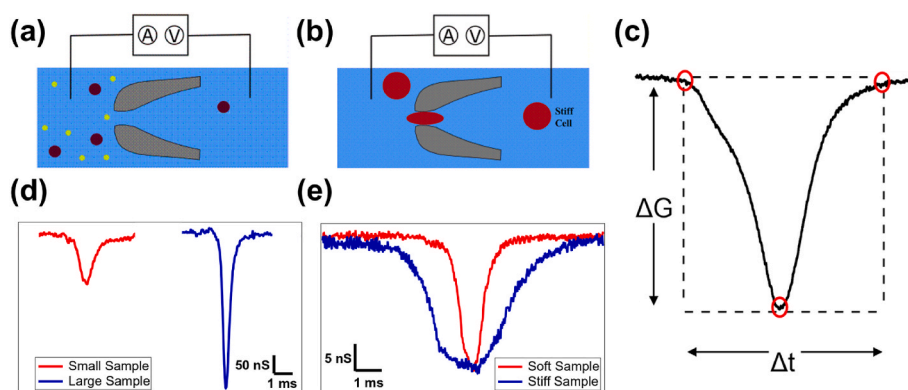


**Fig. 1.** Schematic of electrofluidic device detection principle and signals for measurement of stiffness and size through the micropore device. (a) and (b) shows the schematics of cells translocating through a free flight and a constricted micropore device respectively. (c) A representative electrical event recorded when a cell translocates through the micropore is shown. The start, end, and peak of the event is marked with red circles. The change in conductance ( $\Delta G$ ) and the dwell time ( $\Delta t$ ) for the event is also shown here. (d) Representative events of free-flight experiment for a small (4.3  $\mu\text{m}$  bead, red) and a large (6.0  $\mu\text{m}$  bead, blue) model cells (Polystyrene Beads) translocating through a 7.0  $\mu\text{m}$  pore are shown here. Respective  $\Delta G$  values that correspond to the difference in their sizes can be seen. (e) Representative electrical events of constricted-flight experiments are shown here. A comparison of  $\Delta G$  and  $\Delta t$  signals for a soft (0.5  $\mu\text{M}$  Lat-A treated RBCs, red) and stiff (Native RBCs, blue) samples translocating through a 3.6  $\mu\text{m}$  micropore device is shown here. (For interpretation of the references to colour in this figure legend, the reader is referred to the Web version of this article.)

cantilever (d), and the indentation into the sample (x). The cantilever had a resonant frequency of 15 kHz, length of 225  $\mu\text{m}$ , width of 25  $\mu\text{m}$ , and spring constant of 0.03 N/m. Each cantilever was calibrated for the spring constant (k, pN/nm) and sensitivity ( $\beta$ , nm/V) using the thermal fluctuation mode of the AFM and taking an F-X curve on the glass surface in RPMI, respectively. On each cell, at least 10 F-X curves were recorded with a dwell time of 2 s between consequent curves. The data was recorded at a sample rate of 10 kHz and low pass filtered at 5 kHz, with a total vertical travel distance of 500 nm. During the approach curve, the trigger in deflection value to stop and retrace was set at 100 nm. For F-X curve analysis and stiffness estimation, a custom-written MATLAB code was used to find the cantilever-sample contact point from the force-distance curve, a representative schematic of the contact point is shown in Fig. S9. To ensure that our AFM experiments are well within the hertz model limit and to achieve reproducible fits, an indentation depth of 50 nm was fixed for all curve fits.

### 3. Results and discussion

#### 3.1. Detection of cell volume and cell stiffness in micropore experiments

We first show the two modes (free-flight and constricted-flight) of micropore experiments which detect changes in cell volume and whole-

cell stiffness, respectively. Fig. 2a shows electrical events corresponding to free-flight translocation of model cells (spherical polystyrene beads) of diameter 6.0 (blue) and 4.3  $\mu\text{m}$  (red), through a micropore of 7.0  $\mu\text{m}$  diameter. While the dwell time ( $\Delta t$ ) corresponds to duration of translocation, the event depth ( $\Delta G_{ff}$ ) of these events correspond to the volume of the translocating model cells. The translocation events, scatter plot ( $\Delta G_{ff}$  vs  $\Delta t$ ) of events of a population of model cells and the  $\Delta G_{ff}$  histograms are shown in Fig. 2a, b, and 2c respectively. We see that model cells of different cell volumes correspond to distinct  $\Delta G_{ff}$  histograms (see Figs. 1d, 2a and 2c). A detailed study of cell volume estimation, its resolution and throughput characteristics has been described elsewhere (Kaushik et al., 2020). In constricted-flight experiments, red blood cells (typical diameter ( $\sim 8 \mu\text{m}$ )) are translocated through a micropore of smaller diameter, using a syringe pump. In Fig. 2d we show concatenated translocation events corresponding to native (blue) and soft (red, LatA treated) RBCs, translocating through a 3.6  $\mu\text{m}$  micropore. The changes in event depths ( $\Delta G_{cf}$ ) and event duration ( $\Delta t$ ) is shown as a scatter plot in Fig. 2e. We see that in constricted-flight experiments, the event duration ( $\Delta t$ ) corresponds to whole cell stiffness that allows the cells to squeeze through the constriction. Cells of different stiffness, as shown in Fig. 2f, are identified with their distinct  $\Delta t$  histograms. Note that, the micropores are fabricated manually under optical visualization of the microscope connected to the Microforge instrument, leading to

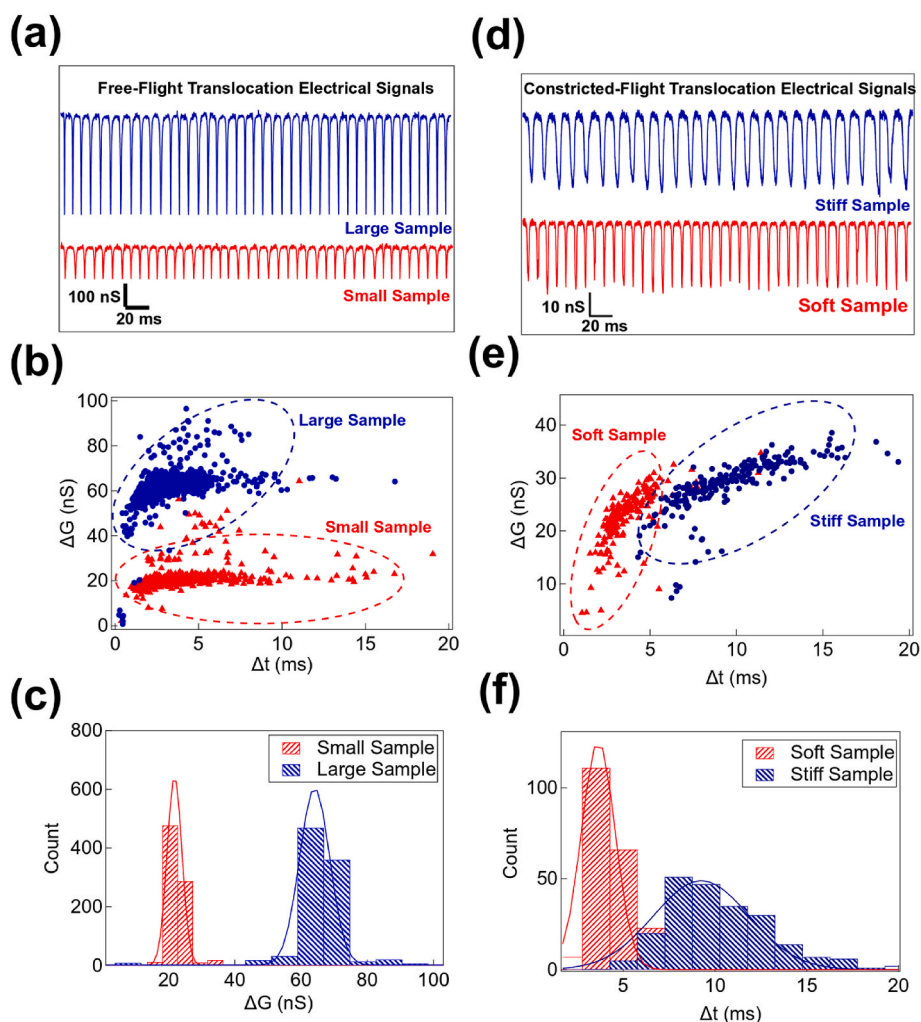


**Fig. 2. Demonstration of cell volume and stiffness detection using electrofluidic devices.** (a), (b) and (c) show translocation electrical signals,  $\Delta G$  vs  $\Delta t$  scatter plot, and the  $\Delta t$  histograms for 6.0  $\mu\text{m}$  (blue) and 4.3  $\mu\text{m}$  (red) polystyrene beads recorded using a 7.0  $\mu\text{m}$  micropore device respectively. (d), (e) and (f) show translocation electrical signals,  $\Delta G$  vs  $\Delta t$  scatter plot, and the  $\Delta t$  histograms for Native (blue) and 1.0  $\mu\text{M}$  Lat-A treated (red) RBCs were recorded using a 3.6  $\mu\text{m}$  micropore device respectively. (For interpretation of the references to colour in this figure legend, the reader is referred to the Web version of this article.)

pore diameter accuracy of  $\pm 1 \mu\text{m}$ . Later in the text, we show that the device functionality is qualitatively reproducible with the current fabrication process (see Fig. 4a). Moreover, when sample properties are compared, they are quantified on the same micropore device to eliminate any pore-to-pore variation.

### 3.2. Measurement of varying cell stiffness of RBCs

Next, we show constricted-flight measurement of RBCs that are softened to varying degree using the Lat-A drug. Latrunculin A is known to soften cells, in a concentration dependent manner, by binding to actin monomers near the nucleotide-binding cleft and thus sequestering them from actin polymerization in cells (Braet et al., 1996; Fujiwara et al., 2018). This actin-spectrin scaffolding inside the inner membrane of RBCs gets affected due to the depolymerization of actin, which results in the softening of the entire cell (Gokhin et al., 2015; Gokhin and Fowler, 2017; Letierrier and Pullarkat, 2022). Red blood cells from a healthy donor were incubated in different concentrations of Lat-A and the effect of the drug on RBC sample was measured with constricted-flight experiments using micropores. Note, to avoid device-dependent artifacts, experiments with all Lat-A concentrations were performed, back-to-back, on the same device, with thorough washing of fluid-cell between experiments and randomizing the order of Lat-A concentrations. The translocation events on a  $3.6 \mu\text{m}$  diameter constricted micropore are shown in Fig. 3a. It shows that the effect of reduced whole cell stiffness by incubation in Lat-A, translates to longer translocation times ( $\Delta t$ ). Since Lat-A treated RBCs show no change in cell size/volume (see Fig. S10), the increase in constricted-flight translocation times is attributed to reduction in cell stiffness. We confirmed this result with constricted flight experiments done on multiple devices. The constricted flight  $\Delta t$  data for RBCs treated with five different Lat-A concentrations and measured using 3.0, 3.2, 3.6, 3.8, and  $3.9 \mu\text{m}$  diameter micropores is shown in Fig. 3b. We observe a systematic decrease in the  $\Delta t$  with the increasing Lat-A concentrations.

### 3.3. RBC elastic modulus estimation

The reduction in whole cell stiffness by Lat-A is well documented (Braet et al., 1996; Fujiwara et al., 2018; Vargas-Pinto et al., 2013; Fischer et al., 2020; Kubitschke et al., 2017; Stack et al., 2018). However, to compare the cell stiffness changes in the cell population being measured using the micropore, we directly quantify the change in their elastic modulus using an atomic force microscope (AFM) mounted on an inverted optical microscope. The AFM force measurements were performed on RBCs oriented horizontally, as shown in Fig. S8. For reproducible results, the AFM cantilever with a microsphere attached to the tip was optically aligned on top of the red blood cell. Force-indentation curves were obtained by pressing the tip-bound microsphere against the cell (see Fig. S9). From the force indentation curves (see Fig. 3c), the elastic modulus of RBCs was estimated using the Hertz Model given by:

$$F = \frac{4\sqrt{R_C}}{3} \frac{E}{1-\nu^2} \delta^{\frac{3}{2}} \quad (1)$$

Here,  $F$ ,  $R_C$ ,  $E$ ,  $\nu$ , and  $\delta$  are force, the radius of the spherical probe, the elastic modulus of the sample, Poisson's ratio of RBC and indentation respectively. In Fig. 3c, the force-indentation curves with the respective Hertz model fits for untreated RBC (black) and then same cell treated with  $0.50 \mu\text{M}$  (green) and  $1.0 \mu\text{M}$  (red) Lat-A drug, successively, are shown. The experiment is repeated for all Lat-A concentrations and the resulting changes in the elastic modulus of that same red blood cell is plotted in Fig. 3d inset. These experiments are repeated on multiple cells. The Lat-A concentration-wise average (overall measured cells) of the AFM measurement of cell elasticity is plotted in Fig. 3d. As expected, AFM measurements show systematic decrease in elastic modulus ( $E$ , kPa) with increasing Lat-A concentrations.

### 3.4. Empirical correlation between constricted micropore dwell times and cellular stiffness

We next establish qualitative dependence of dwell times ( $\Delta t$ , ms) of constricted-flight micropore experiments of RBCs with AFM-based

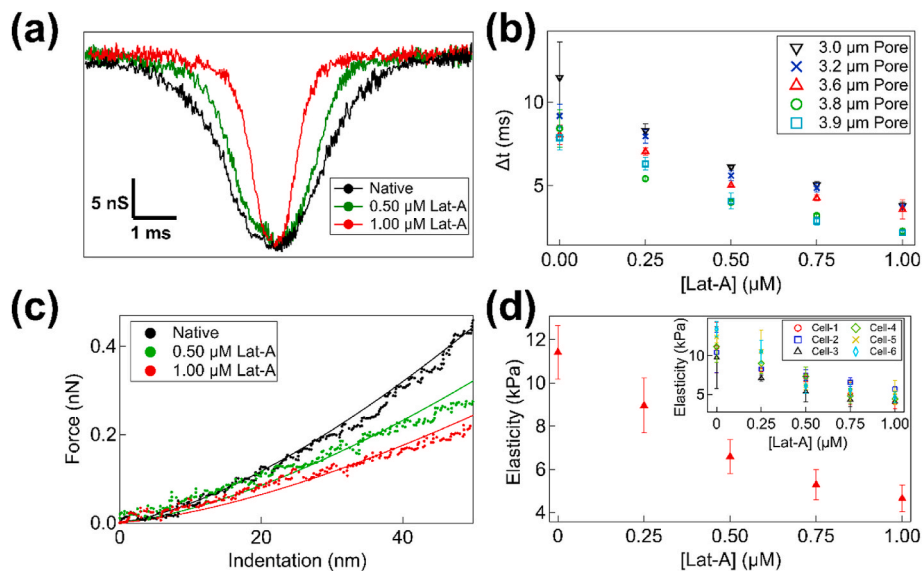


**Fig. 3.** Effect of the actin inhibitor drug (Latrunculin-A) on the stiffness of red blood cells. (a) Translocation electrical signals for healthy RBCs (black) and RBCs treated with  $0.50 \mu\text{M}$  (green) and  $1.0 \mu\text{M}$  Lat-A drug, showing a decrease in the dwell time ( $\Delta t$ ) translocating through the  $3.6 \mu\text{m}$  micropore device. (b) Here we present the constricted flight dwell time ( $\Delta t$ ) data, measured in  $3.0$ ,  $3.2$ ,  $3.6$ ,  $3.8$ , and  $3.9 \mu\text{m}$  diameters micropores, for red blood cells treated with different concentration of Lat-A. For this experiment, RBC samples were obtained from a healthy donor (with  $90.2 \text{ fL}$  mean corpuscular volume, MCV, from pathology test). (c) AFM force-distance curve with the respective Hertz model fits (equation (1)) for healthy RBCs (black) and RBCs treated with  $0.50 \mu\text{M}$  (green) and  $1.0 \mu\text{M}$  Lat-A drug. (d) The elasticity of red blood cells, incubated with different amounts of Lat-A as measured using the AFM force spectroscopy is shown here. A spherical ( $4.5 \mu\text{m}$ ) cantilever having a spring constant of  $0.03 \text{ N/m}$  was used for the study. The inset shows the effect of Lat-A on six individual cells. (For interpretation of the references to colour in this figure legend, the reader is referred to the Web version of this article.)

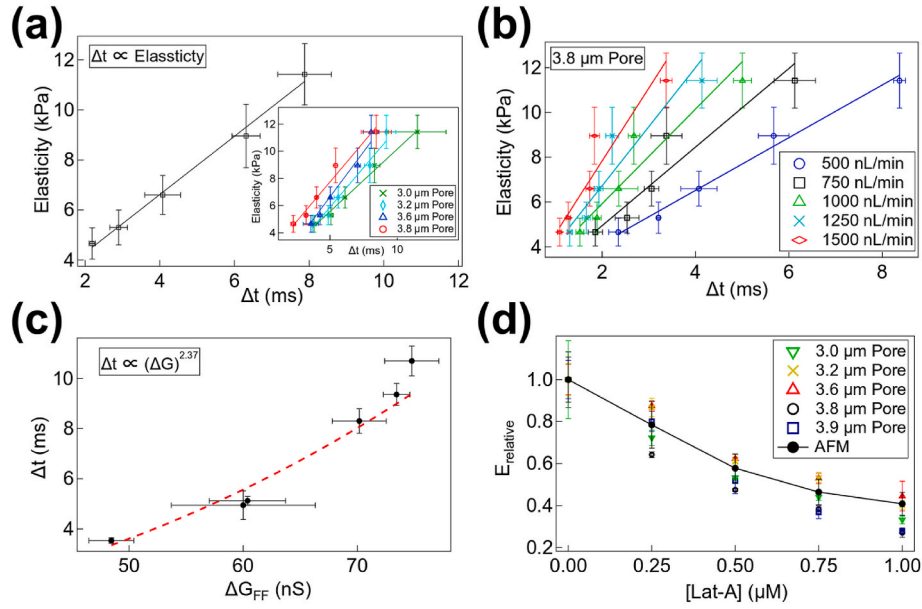


**Fig. 4. Empirical formulation for modeling the cellular stiffness using the electrofluidic experimental data.** (a) The elasticity of RBCs obtained from the AFM is plotted with the  $\Delta t$  measurements of electrofluidic devices for cells treated with different concentrations of Lat-A. Note that there is a linear dependency of dwell time on the RBCs elasticity for all the micropores of different diameters used in the experiment. (b) The linear relationship between the elasticity of RBCs treated with different Lat-A concentrations with the constricted  $\Delta t$  measurements at different flow-rates using a 3.8  $\mu\text{m}$  micropore device is shown (c) Red blood samples were acquired from different donors and, a 4.3 and 8.0  $\mu\text{m}$  micropore device was used for constricted and free flight experiments respectively. Note that the constricted  $\Delta t$  has a power law dependence on the free flight  $\Delta G$  with an exponent value of 2.37, where the free flight  $\Delta G$  corresponds to the volume of the cells. (d) The relative elasticity values from micropore and AFM experiments are shown here, note that both the data show similar trend for RBCs treated with different Lat-A concentrations. (For interpretation of the references to colour in this figure legend, the reader is referred to the Web version of this article.)

elastic modulus ( $E$ , kPa) measurements. We note that both the micropore  $\Delta t$  measurements (Fig. 3b), as well as their elastic modulus (Fig. 3d), decrease similarly with different concentrations of Lat-A. This direct dependence is plotted in Fig. 4a. We find, empirically, linear dependence of constricted-flight translocation time,  $\Delta t$ , on the elastic modulus,  $E$ , of the translocating cell. We confirm this dependence for multiple devices with different micropore diameters (3.0, 3.2, 3.6, 3.8, and 3.9  $\mu\text{m}$ ) (see Fig. 4a inset). The values of the linear fits are summarized in Table S1, with an average slope of  $1.15 \pm 0.12$ . This suggests that the RBCs elastic modulus ( $E$ ) and the constricted-flight micropore dwell times are directly proportional:

$$\Delta t \propto E \quad (2)$$

The constricted-flight dwell times may depend on the flow rate ( $Q$ , nL/min) (See Figs. S11 and S12). We find that the linear dependence of  $\Delta t$  on the elastic modulus ( $E$ ) is maintained across multiple  $Q$  values (see Fig. 4b). The dwell time for constricted-flight experiments may also depend on the cell size/volume. Although Lat-A doesn't change the cell volume (Fig. S10), this dependence should be considered when RBC from different donors (see below) is compared. To establish this dependence, we acquired red blood cells from different healthy donors, with different mean cell volumes (as measured from pathology reports) and compared their free-flight  $\Delta G_{FF}$  (corresponds to cell volume) (Kaushik et al., 2020) values to their constricted-flight  $\Delta t$  values. We used 4.3 and 8.0  $\mu\text{m}$  micropore devices for constricted and free flight experiments respectively and the measured data is shown in Fig. 4c. The dotted red line is a power-law fit giving the following relationship:

$$\Delta t \propto (\Delta G_{FF})^{2.37} \quad (3)$$

Here, since all RBC samples are from different healthy donors, we assume they differ only in their cell volume. The constricted-flight dwell times,  $\Delta t$ , also depend on the experimental parameters (such as fluid flow rate ( $Q$ ), applied voltage ( $V_m$ ), fluid viscosity ( $\mu$ ) and temperature ( $T$ )) as well as geometrical parameters of (Length ( $L_p$ ) and Diameter ( $D_p$ ))

of the micropore).

On combining all the parameters discussed above, we get an empirical relation:

$$\Delta t \propto E \times (\Delta G_{FF})^{2.37} \times f(L_p, V_m, D_p, Q, \mu, T) \quad (4)$$

The expression for  $\Delta t$  can now be written as:

$$\Delta t = k \times E \times (\Delta G_{FF})^{2.37} \quad (5)$$

Here,  $k$  is the proportionality constant. Note, that experiments that compare control and sample cells are performed using the same micropore (i.e. same  $L_p$  and  $D_p$ ), a constant fluid flow (i.e. same  $Q$  and  $\mu$ ), and experimental and sample incubation temperature ( $T$ ). This allows all the terms in  $f(L_p, D_p, V_m, Q, \mu, T)$  to be absorbed into the proportionality constant  $k$  in equation (5). We can now, directly measure the change in the elastic modulus of unknown samples, relative to the elastic modulus of a control sample:

$$E_{relative} = \frac{E_{Sample}}{E_{Control}} = \left( \frac{\Delta t_{Sample}}{\Delta t_{Control}} \right) \times \left( \frac{\Delta G_{FF}^{Control}}{\Delta G_{FF}^{Sample}} \right)^{2.37} \quad (6)$$

Here,  $E_{relative}$  is the ratio of the elasticities of the sample and the control cells, whereas  $\Delta t$  and  $\Delta G_{FF}$  are the constricted-flight dwell times and free-flight conductance change values respectively. We use the above empirical equation to estimate the relative change in RBC cell stiffness upon Lat-A treatment. The  $E_{relative}$  estimated for Lat-A treated RBC cells is shown in Fig. 4d. In the same plot, we also show the change in elastic modulus (measured relative to the native RBC sample) as measured by the AFM for RBCs treated with the same concentrations of Lat-A. The excellent agreement of our micropore empirical approach with the AFM data shown in Fig. 4d provides strength to our experimental procedure to estimate changes in the elastic modulus of a sample relative to a control.

### 3.5. Screening SCD patients based on RBC stiffness

Finally, we apply our micropore device and analysis to compare translocation experiments performed on RBC samples drawn from a healthy donor and sickle cell disease patients, at the hospital (see setup image in Fig. S15). The two samples, when measured using the same device, showed a clear distinction that the SCD patient RBCs translocated much slower than the healthy RBCs. This indicates that the SCD RBCs are stiffer than the native healthy RBC cells. Representative plots of the raw electrical translocation signals, the  $\Delta G_{cf}$  vs  $\Delta t$  scatter plots, and the  $\Delta t$  histograms (see Fig. 5a, b, and 5c respectively), show a clear distinction between the RBC samples from a healthy donor (blue) and an SCD patient (red) when detected using a constricted micropore device ( $4.6 \mu\text{m}$ ). We measure RBC stiffness for 10 SCD patients (available during the time of this study, see Table S4). For these experiments, the samples were collected from patients and a healthy donor and the respective RBCs were suspended in RPMI buffer. This was to ensure that every SCD patient's RBC data had in-situ control of the healthy donor RBCs on the same device and experimental conditions. The RBCs were imaged (see Fig. S16) and split into two batches for simultaneous free-flight (to compare cell volumes) and constricted-flight (to compare cell stiffness) experiments. The constricted-flight  $\Delta t$  bar-plot, the  $\Delta t$  histograms,  $\Delta t$  vs  $\Delta G$  scatter plots, and the free-flight  $\Delta G_{ff}$  bar plots for patient and control samples for all the experiments performed on SCD patients at the hospital are shown in Figs. S17–S22 along with the respective constricted and free-flight micropore images used for the experiment. A complete summary of all the micropore experiments

performed in the hospital and relevant pathology data from patients and the healthy donor is provided in Table S4. We note that, in general, RBCs from SCD patients have a larger distribution in cell volume (as measured by  $\Delta G_{ff}$ ) and take a longer time to translocate through the constricted geometry of the micropore (as measured by constricted-flight dwell times,  $\Delta t$ ). This is shown in Fig. 5d. Here we show the scatter plot of normalized constricted-flight  $\Delta t$  and  $\Delta G_{ff}$  showing distinct populations for SCD patients (red dotted region) and healthy donors (blue dotted region). Note that the data shown in Fig. 5d is normalized with a single control (healthy) donor (black triangle). The summary of the constricted-flight  $\Delta t$  values and the normalized  $\Delta t$  estimated for each patient w.r.t the control is shown in Fig. S23. We then estimate the relative elastic modulus ( $E_{relative}$ ) of patient RBCs using equation (6) and the data is shown in Table S5 and Fig. 5e. The  $E_{relative}$  plot demonstrates that the SCD patient RBCs are, in general, always stiffer compared to the healthy donor RBCs by a factor of 2–4 and our electrofluidic device detects the SCD patient RBCs with high signal-to-noise ratio and throughput. Since we have HbS% values of the SCD patients from the HPLC-based pathology tests, we compared the relative elastic modulus of the RBCs of all the SCD patients of this study with their HbS % values in Fig. 5f. We note that other than two data points (possibly belonging to Sickle Cell Trait patients, HbAS trait) the inset of Fig. 5f shows a linear relationship of  $E_{relative}$  with the HbS% content in the cell. We note that given the low patient number of this study, this linear relationship is only empirical.

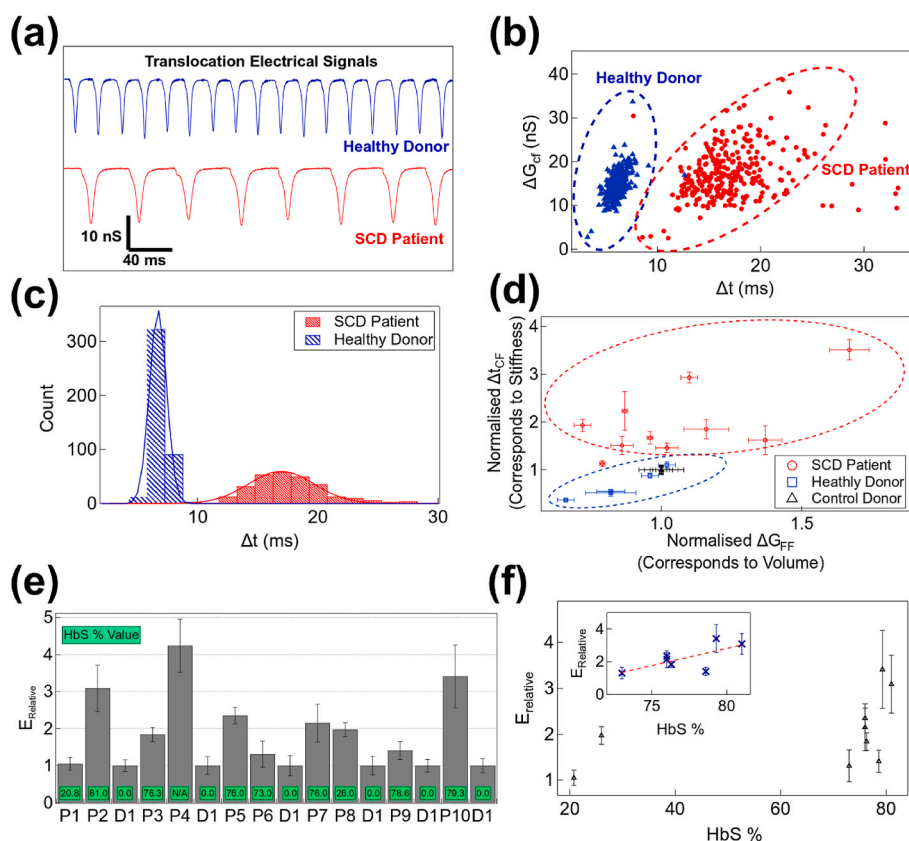


**Fig. 5.** Cellular stiffness estimation of sickled RBCs of the SCD patients using electrofluidic devices. (a), (b) and (c) show translocation electrical signals,  $\Delta G$  vs  $\Delta t$  scatter plot, and the  $\Delta t$  histograms for RBCs from a healthy donor (blue) and an SCD patient (red) recorded using a  $4.6 \mu\text{m}$  micropore device respectively (d) Scatter plot of Normalized  $\Delta t$  and  $\Delta G$  from Constricted and free flight experiments respectively, showing distinct signals for SCD patients (red circles), Healthy donors (blue squares), and Control donors (black triangles). (e) shows the bar plot of relative elasticity empirically estimated according to equation (6) respectively. (f) Shows the relative elasticity of the SCD patient's samples plotted with their respective HbS % values obtained from the HPLC test. Inset shows an increasing trend of relative elasticity for SCD patients with higher HbS% values. (For interpretation of the references to colour in this figure legend, the reader is referred to the Web version of this article.)

#### 4. Conclusions

In this work, we fulfill the niche requirement of whole cell stiffness quantification at high resolution and throughput and demonstrate its application by screening RBCs of sickle cell disease patients. First, we demonstrate the cell volume and stiffness detection principles, using the free-flight and constricted-flight modes of our electro-fluidic micropore device, respectively. We, then show that, for a soft sample like a biological cell, the measured dwell time ( $\Delta t$ ) through a constricted micropore, corresponds to the stiffness of the sample. For this, we treat healthy RBC cells with different concentrations of Latrunculin A drug which artificially softens the whole cell. The elastic moduli and the dwell time ( $\Delta t$ ) values of LatA-treated cells measured simultaneously, using AFM and micropore respectively, helped us calibrate a linear relationship between the RBC cell's elastic moduli and the dwell times ( $\Delta t$ ) measured using different micropore devices; the slope was  $1.15 \pm 0.12$  at our experimental conditions. We established an empirical expression for relative elasticity (equation (6)) of samples w.r.t to a control sample taken from a healthy donor. Finally, we demonstrated the application of our micropores for screening Sickle Cell Disease (SCD) patients. Micropore translocation experiments were performed to compare RBCs from healthy and SCD patients. The micropore parameters ( $\Delta t$  values) of RBCs from the SCD patients were distinctively different from those of healthy donors. The relative elasticity of all patients was found to be always more than that of a healthy donor (see Fig. 5e). We also found a weak linear relationship between the relative elasticity and the HbS% for SCD patients. It is important to note that the medication regimen of the participating patients could not be accounted for in our study. Our approach can identify SCD RBCs based on mechanical changes even in the absence of or way before the visual signatures of sickling of the blood cells, hence a better tool for population-wide preliminary screening. Although, any mechanical abnormality found in a sample doesn't confirm a sickle cell disease diagnosis, but indicates a possible haematological condition that would require further investigation. Ultimately, the electrofluidic mechanotyping of cells demonstrated here may have widespread applications; including investigation and optimization of mechanical properties of vesicles and hydrogels in determining their performance and durability in various diagnostic and drug delivery systems respectively. Our system may also have applications in circulating tumor cell detection, and low-cost hematological screening in veterinary sciences.

#### CRedit authorship contribution statement

**Saurabh Kaushik:** Writing – review & editing, Writing – original draft, Software, Methodology, Formal analysis, Data curation. **Arkab-rata Mishra:** Writing – review & editing, Methodology, Data curation. **Roshan Ross:** Writing – review & editing, Resources, Methodology. **Sweta Srivastava:** Writing – review & editing, Resources, Investigation, Conceptualization. **Cecil R. Ross:** Writing – review & editing, Supervision, Methodology, Investigation, Conceptualization. **Gautam V. Soni:** Writing – review & editing, Writing – original draft, Supervision, Software, Resources, Project administration, Methodology, Investigation, Funding acquisition, Formal analysis, Data curation, Conceptualization.

#### Declaration of competing interest

The authors declare that they have no known competing financial interests or personal relationships that could have appeared to influence the work reported in this paper.

#### Acknowledgements

We acknowledge funding from DST – India (TDP/BTD/08/2019) and internal funding from RRI. We are thankful for assistance from RRI

machine workshop, SEM and AFM facility. We also acknowledge St. Johns Medical College and Hospital for IEC review and permissions.

#### Appendix A. Supplementary data

Supplementary data to this article can be found online at <https://doi.org/10.1016/j.biosx.2025.100616>.

#### Data availability

Data will be made available on request.

#### References

- Abdel-Hadi, L., Ventura, Carmenate Y., Marx Castillo-Aleman, Y., Sheikh, S., Zakaria, A., Phillips, J., 2023. Treatment of sickle cell disease-options and perspective. *Am J Blood Res.* 13 (2), 61–70.
- Adamo, A., Sharei, A., Adamo, L., Lee, B., Mao, S., Jensen, K.F., 2012. Microfluidics-based assessment of cell deformability. *Anal. Chem.* 84 (15), 6438–6443. <https://doi.org/10.1021/ac300264v>.
- Aich, A., Lamarre, Y., Sacomani, D.P., Kashima, S., Covas, D.T., de la Torre, L.G., 2021. Microfluidics in sickle cell disease research: state of the art and a perspective beyond the flow problem. *Front. Mol. Biosci.* 7. <https://doi.org/10.3389/fmolb.2020.558982>.
- Albertolle, M.E., 2017. Characteristics of a rapid, point-of-care lateral flow immunoassay for the diagnosis of sickle cell disease. *Physiol. Behav.* 176 (5), 139–148. <https://doi.org/10.1002/ajh.24232.Characteristics>.
- Alli, N.A., Loonat, S.B., 2010. Solubility tests and the peripheral blood method for screening for sickle cell disease. *S. Afr. Med. J.* 100 (10), 616. <https://doi.org/10.7196/samj.4419>.
- Arishi, W.A., Al-hadrami, H.A., Zourob, M., 2021. Techniques for the detection of sickle cell disease: a review. *Micromachines* 12 (5), 1–22. <https://doi.org/10.3390/mi12050519>.
- Bhatia, H.M., Rao, V.R., 1986. *Genetic Atlas Of the Indian Tribes*. Institute of Immunohaematology. Indian Council of Medical Research.
- Braet, F., De Zanger, R., Jans, D., Spector, I., Wisse, E., 1996. Microfilament-disrupting agent latrunculin A induces an increased number of fenestrae in rat liver sinusoidal endothelial cells: comparison with cytochalasin B. *Hepatology* 24 (3), 627–635. <https://doi.org/10.1053/jhep.1996.v24.pm0008781335>.
- Brandow, A.M., Liem, R.I., 2022. Advances in the diagnosis and treatment of sickle cell disease. *J. Hematol. Oncol.* 15 (1), 1–13. <https://doi.org/10.1186/s13045-022-01237-z>.
- Byun, S., Son, S., Amodei, D., et al., 2013. Characterizing deformability and surface friction of cancer cells. *Proc. Natl. Acad. Sci. USA* 110 (19), 7580–7585. <https://doi.org/10.1073/pnas.1218806110>.
- Desai, D., Dhanani, H., 2012. Sickle cell disease: history and origin. *Internet J. Hematol.* 1 (2). <https://doi.org/10.5580/499>.
- Fischer, T., Hayn, A., Mierke, C.T., 2020. Effect of nuclear stiffness on cell mechanics and migration of human breast cancer cells. *Front. Cell Dev. Biol.* 8 (May), 1–18. <https://doi.org/10.3389/fcell.2020.00393>.
- Fisher, S.I., Haga, J.A., Castleberry, S.M., Hall, R.B., Thompson, W.C., 1997. Validation of an automated HPLC method for quantification of hemoglobin S. *Clin. Chem.* 43 (9), 1667–1669. <https://doi.org/10.1093/clinchem/43.9.1667>.
- Fujiwara, I., Zweifel, M.E., Courtemanche, N., Pollard, T.D., 2018. Latrunculin A accelerates actin filament depolymerization in addition to sequestering actin monomers. *Curr. Biol.* 28 (19), 3183–3192.e2. <https://doi.org/10.1016/j.cub.2018.07.082>.
- Gokhin, David S., Fowler, Velia M., 2017. Feisty filaments: actin dynamics in the red blood cell membrane skeleton. *Curr. Opin. Hematol.* 23 (3), 206–214. <https://doi.org/10.1097/MOH.0000000000000227>.
- Gokhin, D.S., Nowak, R.B., Khoory, J.A., De La Piedra, A., Ghiran, I.C., Fowler, V.M., 2015. Dynamic actin filaments control the mechanical behavior of the human red blood cell membrane. *Mol. Biol. Cell* 26 (9), 1699–1710. <https://doi.org/10.1091/mbc.E14-12-1583>.
- Gossett, D.R., Tse, H.T.K., Lee, S.A., et al., 2012. Hydrodynamic stretching of single cells for large population mechanical phenotyping. *Proc. Natl. Acad. Sci. USA* 109 (20). <https://doi.org/10.1073/pnas.1200107109>.
- Ilyas, S., Simonson, A.E., Asghar, W., 2020. Emerging point-of-care technologies for sickle cell disease diagnostics. *Clin. Chim. Acta* 501, 85–91. <https://doi.org/10.1016/j.cca.2019.10.025>.
- Ito, H., Kaneko, M., 2020. On - chip cell manipulation and applications to deformability measurements. *ROBOMECH Journal*. <https://doi.org/10.1186/s40648-020-0154-x>. Published online.
- Ji, C., Chen, Y.H., Peng, Z., 2024. Predicting vaso-occlusion in sickle cell disease by microfluidics and modeling. *Blood* 144 (Suppl. 1). <https://doi.org/10.1182/blood-2024-207628>, 5275–5275.
- Kato, G.J., Piel, F.B., Reid, C.D., et al., 2018. Sickle cell disease. *Nat. Rev. Dis. Primers* 4, 1–22. <https://doi.org/10.1038/nrdp.2018.10>.
- Kaushik, S., Mahadeva, M., Murugan, K.D., Sundaramurthy, V., Soni, G.V., 2020. Measurement of alcohol-dependent physiological changes in red blood cells using resistive pulse sensing. *ACS Sens.* 5 (12), 3892–3901. <https://doi.org/10.1021/acssensors.0c01302>.

- Kaushik, S., Selvanathan, P., Soni, G.V., 2022. Customized low-cost high-throughput amplifier for electro-fluidic detection of cell volume changes in point-of-care applications. *PLoS One* 17 (4), e0267207. <https://doi.org/10.1371/journal.pone.0267207>.
- Kim, J., Han, S., Lei, A., et al., 2018. Characterizing cellular mechanical phenotypes with mechano-node-pore sensing. *Microsyst Nanoeng* 4 (1). <https://doi.org/10.1038/MICRONANO.2017.91>.
- Kubitschke, H., Schnauss, J., Nnetu, K.D., Warmt, E., Stange, R., Kaes, J., 2017. Actin and microtubule networks contribute differently to cell response for small and large strains. *New J. Phys.* 19 (9). <https://doi.org/10.1088/1367-2630/aa7658>.
- Letierrier, C., Pullarkat, P.A., 2022. Mechanical role of the submembrane spectrin scaffold in red blood cells and neurons. *J. Cell Sci.* 135 (16), 1–9. <https://doi.org/10.1242/jcs.259356>.
- Liu, J., Qiang, Y., Du, E., 2017. Measurement of electrical properties of sickle cells from electrical impedance of cell suspension. *ASME Int. Mech. Eng. Congress Exposition, Proc. (IMECE)* 3, 1–6. <https://doi.org/10.1115/IMECE2017-71734>.
- Liu, J., Qiang, Y., Alvarez, O., Du, E., 2018. Electrical impedance microflow cytometry with oxygen control for detection of sickle cells. *Sensor. Actuator. B Chem.* 255, 2392–2398. <https://doi.org/10.1016/j.snb.2017.08.163>.
- Liu, Jia, Qiang, Yuhao, Alvarez, OE Du, 2019. Electrical impedance characterization of erythrocyte response to cyclic hypoxia in sickle cell disease. *ACS Sens.* 26, 1783–1790. <https://doi.org/10.1021/acssensors.9b00263>.
- Marcus, S.J., Kinney, T.R., Schultz, W.H., O'Branski, E.E., Ware, R.E., 1997. Quantitative analysis of erythrocytes containing fetal hemoglobin (F cells) in children with sickle cell disease. *Am. J. Hematol.* 54 (1), 40–46. [https://doi.org/10.1002/\(SICI\)1096-8652\(199701\)54:1<40::AID-AJH6>3.0.CO;2-4](https://doi.org/10.1002/(SICI)1096-8652(199701)54:1<40::AID-AJH6>3.0.CO;2-4).
- MoHFW, 2023. National sickle cell anaemia elimination mission. <https://sickle.nhm.gov.in/home>.
- Ndefo, U.A., Maxwell, A.E., Nguyen, H., Chiobi, T.L., 2008. Pharmacological management of sickle cell disease. *P T* 33 (4), 238–243.
- Nyberg, K.D., Scott, M.B., Bruce, S.L., et al., 2016. The physical origins of transit time measurements for rapid, single cell mechanotyping. *Lab Chip* 16, 3330–3339. <https://doi.org/10.1039/C6LC00169F>.
- Nyberg, K.D., Hu, K.H., Kleinman, S.H., Khismatullin, D.B., Butte, M.J., 2017. Quantitative deformability cytometry : rapid , calibrated measurements of cell mechanical properties. *Biophys. J.* 113 (7), 1574–1584. <https://doi.org/10.1016/j.bpj.2017.06.073>.
- Obeagu, E.I., Ochei, K., Okoro, O., 2015. Sickle cell anaemia : a review. *Scholars J. Appl. Med. Sci.* 3, 2244–2252.
- Otto, O., Rosendahl, P., Mietke, A., et al., 2015. Real-time deformability cytometry: On-the-fly cell mechanical phenotyping. *Nat. Methods* 12 (3), 199–202. <https://doi.org/10.1038/nmeth.3281>.
- Ou, C.N., Rognerud, C.L., 2001. Diagnosis of hemoglobinopathies: electrophoresis vs. HPLC. *Clin. Chim. Acta* 313 (1–2), 187–194. [https://doi.org/10.1016/S0009-8981\(01\)00672-6](https://doi.org/10.1016/S0009-8981(01)00672-6).
- Raj, A., Sen, A.K., 2018. Entry and passage behavior of biological cells in a constricted compliant microchannel. *RSC Adv.* 8 (37), 20884–20893. <https://doi.org/10.1039/c8ra02763c>.
- Rees, D.C., Brousse, V.A.M., Brewin, J.N., 2022. Determinants of severity in sickle cell disease. *Blood Rev.* 56 (June), 100983. <https://doi.org/10.1016/j.blre.2022.100983>.
- Serjeant, G.R., 2013. The natural history of sickle cell disease. *Cold Spring Harb Perspect Med* 3 (10), 1–12. <https://doi.org/10.1101/cshperspect.a011783>.
- Shah, N., Beenhouwer, D., Broder, M.S., et al., 2020. Development of a severity classification system for sickle cell disease. *Clin. Outcomes Res.* 12, 625–633. <https://doi.org/10.2147/CEOR.S276121>.
- Sinha, B., Biswas, A., Kaushik, S., Soni, G.V., 2025. Cellular and Nuclear Forces: An Overview. In: Lavelle, C., Le Gall, A. (Eds.), *Molecular Motors. Methods in Molecular Biology*, vol. 2881. Humana, pp. 3–39. [https://doi.org/10.1007/978-1-0716-4280-1\\_1](https://doi.org/10.1007/978-1-0716-4280-1_1).
- Stack, T., Vahabikashi, A., Johnson, M., Scott, E., 2018. Modulation of Schlemm's canal endothelial cell stiffness via latrunculin loaded block copolymer micelles. *J. Biomed. Mater. Res.* 106 (7), 1771–1779. <https://doi.org/10.1002/jbm.a.36376>.
- Stanley Davidson, S., 2014. *Davidson's Principles and Practice of Medicine*. ELSEVIER.
- Tewari, S., Rees, D., 2013. Morbidity pattern of sickle cell disease in India: a single centre perspective. *Indian J. Med. Res.* 138 (SEP), 288–290.
- Tsai, C.H.D., Sakuma, S., Arai, F., Kaneko, M., 2014. A new dimensionless index for evaluating cell stiffness-based deformability in microchannel. *IEEE Transactions on Biomedical Engineering* 61 (4), 1187–1195. <https://doi.org/10.1109/TBME.2013.2296624>.
- Urbanska, M., Muñoz, H.E., Bagnall, J.S., et al., 2020. A comparison of microfluidic methods for high-throughput cell deformability measurements. *Nat. Methods* 17, 587–593. <https://doi.org/10.1038/s41592-020-0818-8>.
- Vargas-Pinto, R., Gong, H., Vahabikashi, A., Johnson, M., 2013. The effect of the endothelial cell cortex on atomic force microscopy measurements. *Biophys. J.* 105 (2), 300–309. <https://doi.org/10.1016/j.bpj.2013.05.034>.
- Xu, Z., Zheng, Y., Wang, X., Shehata, N., Wang, C., Sun, Y., 2018. Stiffness increase of red blood cells during storage. *Microsyst Nanoeng* 4 (1), 1–6. <https://doi.org/10.1038/MICRONANO.2017.103>.
- Xu, Z., Dou, W., Wang, C., Sun, Y., 2019. Stiffness and ATP recovery of stored red blood cells in serum. *Microsyst Nanoeng* 5 (1). <https://doi.org/10.1038/s41378-019-0097-7>.